PCCP

ROYAL SOCIETY OF CHEMISTRY

PAPER

View Article Online
View Journal | View Issue

Cite this: *Phys. Chem. Chem. Phys.*, 2024, **26**, 3912

Nitrogen adsorption on $Nb_2C_6H_4^+$ cations: the important role of benzyne (*ortho*-C_6H_4)†

Feng-Xiang Zhang, Yi-Heng Zhang, Ming Wang and Jia-Bi Ma *

Received 14th November 2023,
Accepted 26th December 2023

DOI: 10.1039/d3cp05524h

rsc.li/pccp

N_2 adsorption is a prerequisite for activation and transformation. Time-of-flight mass spectrometry experiments show that the $Nb_2C_6H_4^+$ cation, resulting from the gas-phase reaction of Nb_2^+ with C_6H_6, is more favorable for N_2 adsorption than Nb^+ and Nb_2^+ cations. Density functional theory calculations reveal the effect of the *ortho*-C_6H_4 ligand on N_2 adsorption. In $Nb_2C_6H_4^+$, interactions between the Nb-4d and C-2p orbitals enable the Nb_2^+ cation to form coordination bonds with the *ortho*-C_6H_4 ligand. Although the *ortho*-C_6H_4 ligand in $Nb_2C_6H_4^+$ is not directly involved in the reaction, its presence increases the polarity of the cluster and brings the highest occupied molecular orbital (HOMO) closer to the lowest occupied molecular orbital (LUMO) of N_2, thereby increasing the N_2 adsorption energy, which effectively facilitates N_2 adsorption and activation. This study provides fundamental insights into the mechanisms of N_2 adsorption in "transition metal–organic ligand" systems.

1. Introduction

Dinitrogen (N_2) is the most significant and abundant source of various N-containing compounds.[1–5] However, the transformation of N_2 at room temperature remains quite challenging due to its chemical inertness, the high HOMO–LUMO energy gap, large triple bond energy (945 kJ mol^{-1}) and lack of a permanent dipole.[6,7] In nature, nodule bacteria efficiently perform biological nitrogen fixation at ambient temperatures.[8] In the condensed phase, enhancing N_2 chemisorption capability on catalyst surfaces is critical for N_2 reduction.[9,10] Recently, metal–organic complexes, such as metal nitrogen heterocyclic compounds and multi-replacement metallocenes, have been reported to adsorb N_2 and break N≡N bonds under mild conditions.[1,11–17] These unsaturated organic ligands act as electron donors to facilitate N_2 adsorption. For example, a diketiminate-supported iron system that progressively activates benzene and N_2 to produce aniline derivatives has been reported.[18] Despite significant progress in N_2 adsorption, the detailed reaction mechanisms and key influencing factors remain unclear. Furthermore, transition metal benzyne (TM-benzyne) complexes usually serve as reactive intermediates in organic synthetic chemistry.[19–22] It is interesting to explore the reactivity of TM-benzyne toward N_2.

Gas-phase studies on "isolated" reactants provide an ideal venue for investigating reaction mechanisms and kinetics at a strictly molecular level.[7,23–26] Recently, some encouraging developments in N_2 activation have been reported in the gas phase studies,[27–31] and the ligand effect significantly affects cluster reactivity. Gas-phase clusters usually contain metal atoms coupled with inorganic ligands, such as oxygen, boron, hydrogen, carbon, sulfur, and so on.[29,32–35] For example, we recently reported that in $NbB_3O_2^-$, the B_3O_2 ligand and the single Nb center can form a dual active site to promote N_2 activation and transformation.[29] In the $NbH_2^-/CO_2/N_2$ system, the NbN_2^- anion is formed by the reaction of NbH_2^- with N_2, and the N≡N triple bond is cleaved with the formation of the C–N bond in the reaction of NbN_2^- with CO_2.[33] Notably, only limited studies are about N_2 absorption and activation mediated by gas-phase ions containing organic ligands.[36–39] He and coworkers recently reported that $Fe_2VC(C_6H_6)^-$ can feasibly break the N≡N triple bond.[39] Considering the high reactivity of TM-benzyne in the condensed-phase reaction, it is crucial to synthesize isolable TM-benzyne ions and investigate their reactivity toward N_2. Meanwhile, there is an urgent need to identify the interaction mechanism between metal atoms and organic ligands, which may influence the N_2 adsorption rate.

In the present work, the gas-phase TM-benzyne cation $Nb_2C_6H_4^+$ is designed and synthesized through the reaction of Nb_2^+ and C_6H_6. We further investigated its reaction with N_2. The presence of the *ortho*-C_6H_4 ligand increases the adsorption rate of N_2 on $Nb_2C_6H_4^+$ compared to bare Nb_2^+. It is ascribed to the greater polarity and higher HOMO energy level in $Nb_2C_6H_4^+$, which favors N_2 adsorption. Exploring typical clusters possessing metal atoms and organic ligands in the gas phase may provide a novel understanding for N_2 adsorption.

Key Laboratory of Cluster Science of Ministry of Education, Beijing Key Laboratory of Photoelectronic/Electrophotonic Conversion Materials, School of Chemistry and Chemical Engineering, Beijing Institute of Technology, Beijing 102488, P. R. China. E-mail: majiabi@bit.edu.cn

† Electronic supplementary information (ESI) available. See DOI: **https://doi.org/10.1039/d3cp05524h**

2. Methods

2.1 Experimental methods

Interactions of ions and reactant gases are investigated using a homemade time-of-flight mass spectrometer (TOF-MS) equipped with a laser ablation ion source, a quadrupole mass filter (QMF), and a linear ion trap (LIT) reactor. Only a concise description of the apparatus is presented here, since details of the experiment have been previously covered in the earlier work.[40–42] The $Nb_{1,2}^+$ cations are generated by laser ablation of a niobium disk target (99.999%) in helium carrier gas at a backing pressure of 3.0 standard atmospheres. A 532 nm laser with a repetition rate of 10 Hz as well as 5–8 mJ/pulse energy is employed. The $Nb_{1,2}^+$ cations are mass-selected by QMF, and then reacted with N_2 seeded in the cooling gas (He) first. The reaction between Nb_2^+ and diluted benzene vapor seeded in the cooling gas (Ar) generates the $Nb_2C_6H_4^+$ cluster. N_2 is then introduced into the LIT to investigate the N_2 adsorption reaction. Finally, the LIT releases reactant and product ions, which are subsequently detected by reflection TOF-MS. The previous study showed that cations were thermally stabilized around (or just approaching) 298.15 K prior to various reactions.[42]

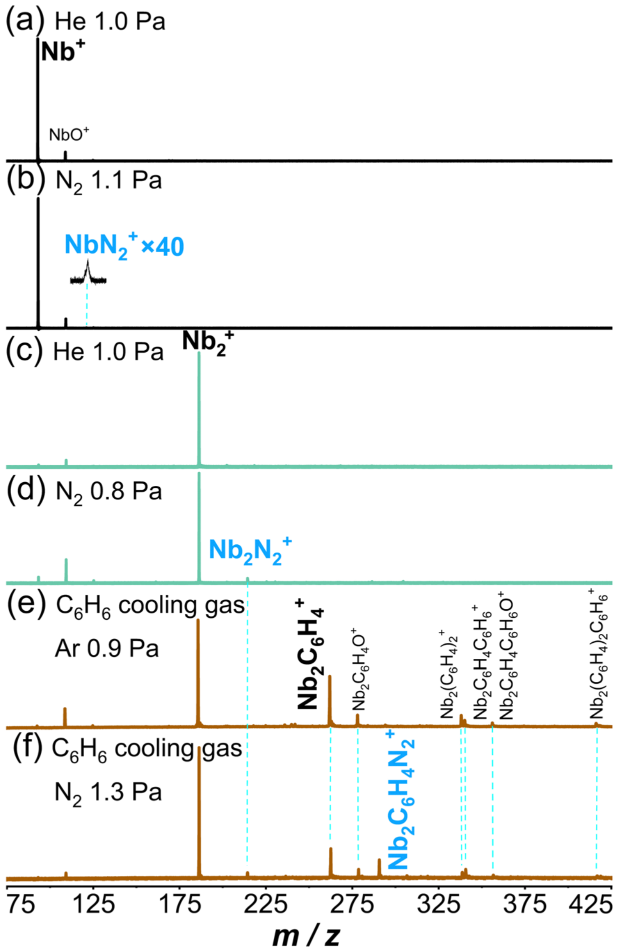

Fig. 1 Time-of-flight (TOF) mass spectra for the reactions of mass-selected Nb^+ (a) and Nb_2^+ (c) with He for 11.4 ms; Nb^+ (b) and Nb_2^+ (d) with N_2 for 13.4 ms and 14.9 ms, respectively; for the reaction of (e) the generated intermediate product $Nb_2C_6H_4^+$ with N_2 (f) for 5.0 ms. The effective reactant gas pressures are shown. In panel (b), the signal magnitude is amplified by a factor of 40 (m/z = 121).

In our experiments, the concentrations of reactant molecules (C_6H_6 or N_2) are much larger than that of reactant cations (Nb^+, Nb_2^+, or $Nb_2C_6H_4^+$). Thus, the pseudo-first-order reaction model (k_1) is assumed in each reaction. The following equation is applied to calculate the rate constant:[42]

$$\ln\frac{I_R}{I_T} = -k_1\frac{P_e}{kT}t_R, \tag{1}$$

in which I_R is the reactant intensity after the reaction and I_T equals the sum of both the reactant and product intensities. In addition, k, t_R, and T correspond to the Boltzmann constant, reaction time, and temperature, respectively. P_e is the effective gas pressure of the reactant in the LIT. Finally, the least squares are used to derive the rate constant of each reaction.[43] The detailed method is described in ref. 43. The errors of t_R (±5%), T (±2%), and P_e (±20%) are also taken into account to estimate the error bars.

2.2 Computational methods

All density functional theory (DFT) calculations are carried out in the Gaussian 09 D.01 program package.[44] The bond dissociation energies of Nb–Nb, Nb–C, Nb–N, N≡N, C–C, C–H, C≡N, H–H and N–H bonds are predicted by 20 tested methods, with the M06L functional agreeing well with the experimental data (Table S1, ESI†), and M06L is more adaptable for the group VB transition metal complexes[45–47] and selected in the present work. Meanwhile, the density functional theory dispersion correction (DFT-D3) is included.[48] The def2-TZVPP basis set is used for the Nb atom,[49,50] and the 6-311+G** basis sets[51–53] are chosen for the H, C, and N atoms. Each initial structure is optimized for various possible spin multiplicities. Flexible scanning and intrinsic reaction coordinates are used to achieve the optimal geometry of intermediates (**I**s) and transition states (**TS**s). Calculations of vibrational frequencies are

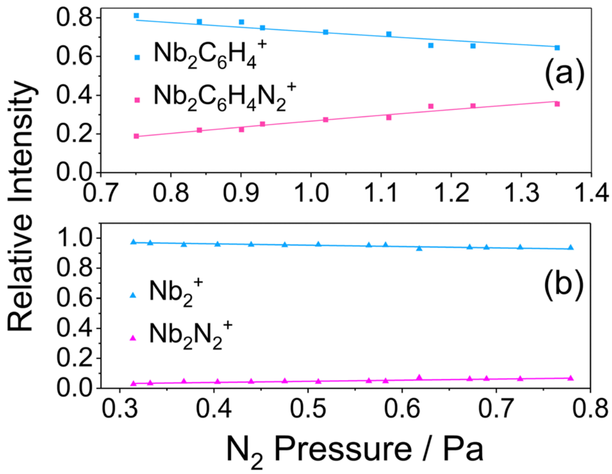

Fig. 2 Variations of the relative intensities of the reactant and product cations in the reactions of $Nb_2C_6H_4^+$ (a) and Nb_2^+ (b) with N_2 with respect to the N_2 pressures for 5 ms and 14.9 ms, respectively. The solid lines are fitted to the experimental data points by using the equations derived from the approximation of the pseudo-first-order reaction model.

used to make sure that **I**s and **TS**s have zero and only one imaginary frequency, respectively. In each reported energy (ΔH_{0K} in eV), the zero-point vibration correction is taken into account. The rate constant of a reaction without an energy barrier is computed by variational transition state theory.[54] NBO 6.0 is used for natural population analysis, which includes natural population analysis (NPA) charge, adaptive natural density partitioning (AdNDP) and percentage of orbital contribution.[55] For the simulated density of states (DOS), the vertical detachment energies (VDEs) of the related clusters have been calculated using the same structures as their initial cations, corresponding to the energy difference between the cluster's Hartree–Fock energies and neutral species. Each peak is the result of the cation capturing an electron. Multiwfn 3.8 is applied to obtain localized orbital locator-π (LOL-π), electrostatic potential (ESP), interaction region indicator (IRI), DOS, and frontier molecular orbital.[56–60]

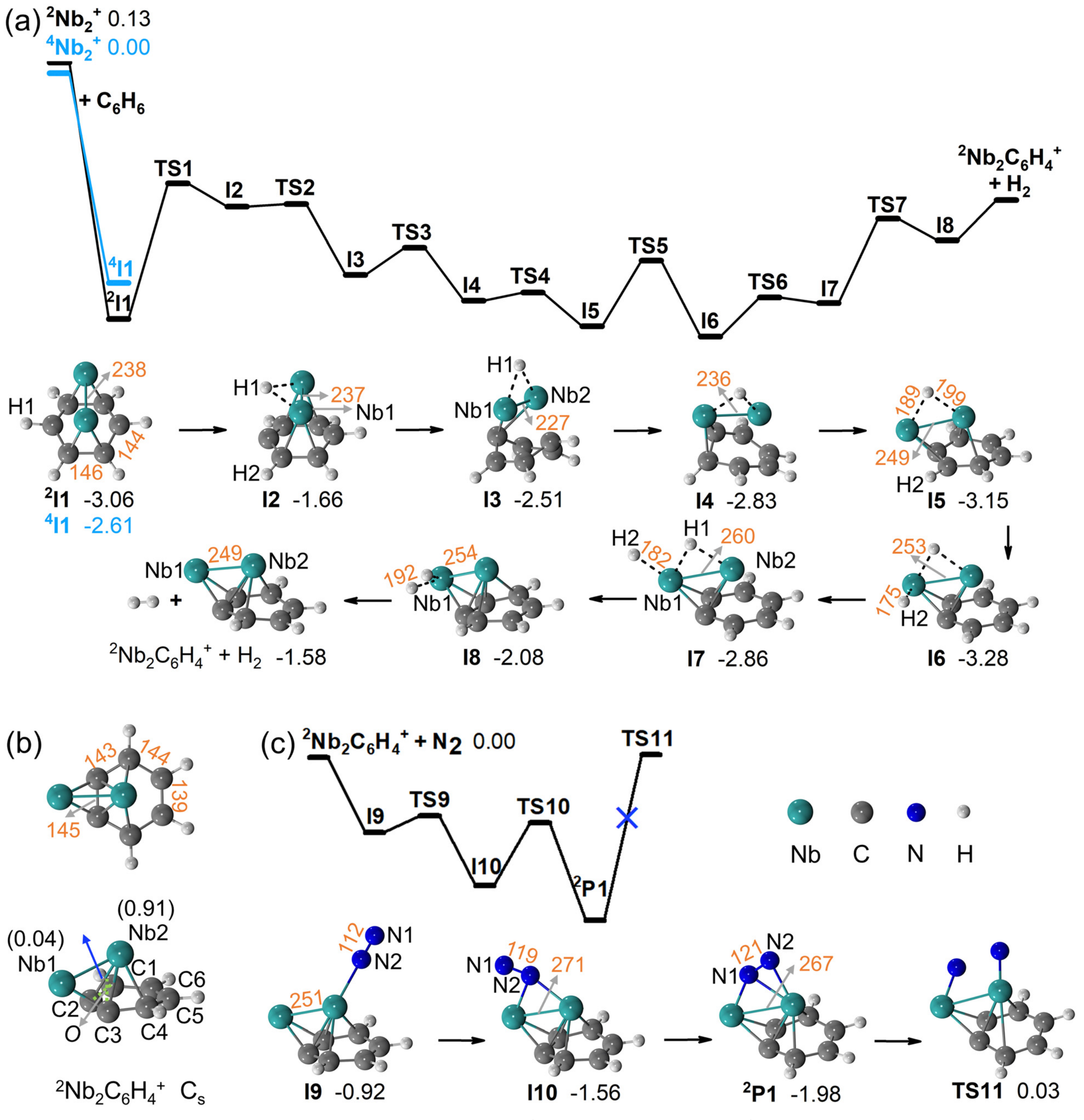

Fig. 3 M06L-calculated potential energy surfaces (PESs) for the (a) Nb_2^+ + C_6H_6, and (c) $Nb_2C_6H_4^+$ + N_2 reactions, and the spin multiplicities are doublet. The zero-point vibration-corrected energies (ΔH_{0K} in eV) of the reaction intermediates, transition states, and products relative to the separated reactants are given. (b) Top (upper panel) and side (bottom panel) views of the optimized global minimum structure of the $Nb_2C_6H_4^+$ cluster. The blue arrow represents the vector direction of dipole moment. The superscripts indicate the spin multiplicities. The bond lengths are given in pm. The values of unpaired spin density distributions are given in parentheses.

3. Results

3.1 Experimental results

As shown in Fig. 1, the Nb^+, Nb_2^+, and $Nb_2C_6H_4^+$ cations generated by laser ablation are mass-selected and subsequently react with N_2 in the LIT reactor. Note that Nb^+ and Nb_2^+ cations show relatively low reactivity toward N_2, Fig. 1b and d, reflected by the low intensities of NbN_2^+ and $Nb_2N_2^+$ even at relatively high N_2 pressures (up to 1.1 Pa and 0.8 Pa) and rather long reaction times (up to 13.4 ms and 14.9 ms). Interestingly, when the organic ligand *ortho*-C_6H_4 is attached on the Nb_2^+ cation, the adsorption rate is increased dramatically. The $Nb_2C_6H_4^+$ clusters can be produced by the mass-selected Nb_2^+ cations (Fig. 1c) reacting with C_6H_6 molecules. As the majority of Nb_2^+ is converted to $Nb_2C_6H_4^+$ (Fig. 1e, reaction (1)), N_2 is pulsed into the LIT reactor. After the reaction with 1.3 Pa N_2 for approximately 5.0 ms, a significant peak corresponding to $Nb_2C_6H_4N_2^+$ is observed in Fig. 1f, suggesting reaction (2). In the mass spectra, the presence of NbO^+, $Nb_2C_6H_4O^+$, and $Nb_2C_6H_4C_6H_6O^+$ peaks arises from reactions of residual water impurities with Nb^+, $Nb_2C_6H_4^+$, and $Nb_2C_6H_4C_6H_6^+$, respectively.

The pseudo-first-order rate constant (k_1) values of reactions (1) and (2) are estimated to be $(1.27 \pm 0.26) \times 10^{-9}$ cm^3 molecule^{-1} s^{-1} and $(2.60 \pm 0.53) \times 10^{-13}$ cm^3 molecule^{-1} s^{-1}, respectively, corresponding to the reaction efficiencies (Φ)[61,62] of 126.7% and 0.04%. The results for Φ are consistent for both the surface charge capture and the average dipole orientation models. The rate for the $Nb_2C_6H_4^+/N_2$ system is 10 times larger than that of the $Nb_2N_2^+/N_2$ [$(2.64 \pm 0.59) \times 10^{-14}$ cm^3 molecule^{-1} s^{-1}], and the presence of the C_6H_4 ligand indeed increases the adsorption rate of N_2. The signal dependence of product ions on N_2 pressures and C_6H_6 are derived and fitted to the experimental data (Fig. 2 and Fig. S1, ESI†).

3.2 Computational results

DFT calculations are performed to obtain the lowest-energy isomers of $Nb_2C_6H_6^+$ (Fig. S2a, ESI†) and $Nb_2C_6H_4^+$ (Fig. S3a, ESI†), and the dehydrogenation mechanism for reaction (1) is shown in Fig. 3a. Nb_2^+ has a quartet spin multiplicity.[63] A spin crossover from the quartet potential energy surface (PES) to the doublet PES potentially takes place during the formation of **I1** ($Nb_2C_6H_6^+$, $\Delta H_{0K} = -2.61$ eV, with respect to the separate reactants). The first hydrogen (H1) transfers from the C_6H_6 unit in **I1** to the Nb atom in $Nb_2C_6H_6^+$ *via* **TS1** to generate **I2**. Then **I3** is formed by rotating H1 to the top of the linear Nb–Nb bond through **TS2**. The relative position of the Nb–Nb unit and C_6H_6 has been changed slightly. In the steps of **I3** → **I4** → **I5**, the Nb1–Nb2–H1 unit is further rotated relative to the C_6H_6 unit. It is emphasized that steps **I3** → **I4** → **I5** are crucial to this reaction process because the direct C–H2 (second hydrogen) bond-breaking in **I2** is difficult. From **I5**, the H2 migrates from the C_6H_6 unit to the Nb1 atom, leading to the formation of intermediate **I6**. *Via* **TS6**, a planar H2–Nb1–Nb2–H1 unit in **I7** is generated by rotating the H2 atom. Two hydrogen atoms bonded with Nb1 are combined to form one H_2 unit in **I8**. Finally, $Nb_2C_6H_4^+$ and H_2 are generated. Thus, the dehydrogenation reaction of $Nb_2C_6H_6^+$ cations is thermodynamically and kinetically favourable. As shown in Fig. 3b, the C2–C3 and Nb–Nb bonds in $Nb_2C_6H_4^+$ are elongated by approximately 20 pm and 47 pm, respectively, in comparison to the separate

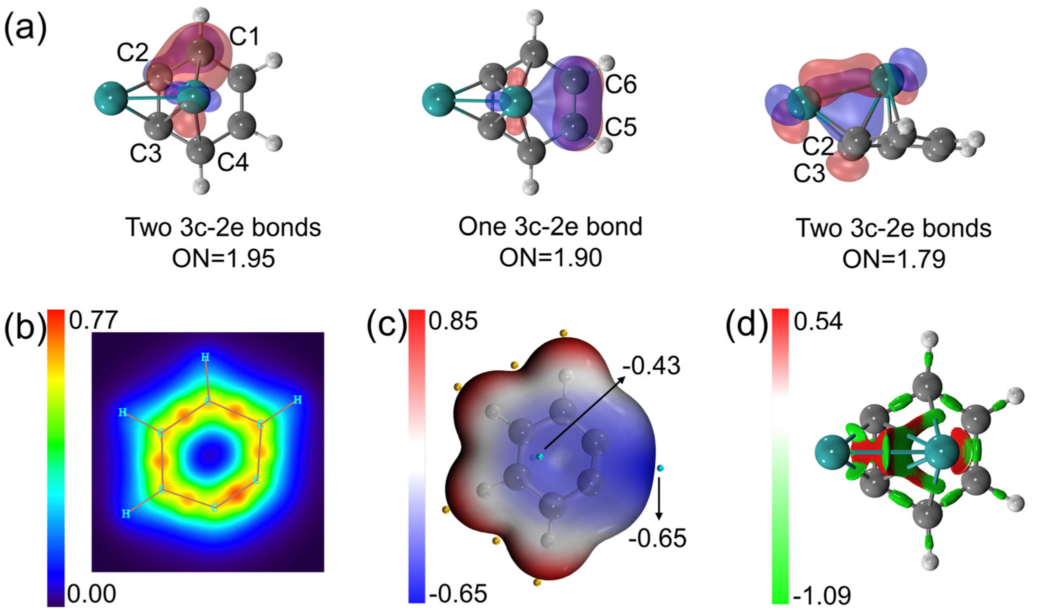

Fig. 4 (a) Adaptive natural density partitioning (AdNDP, unit: *e*) bonding analysis for three-center two-electron (3c–2e) bonds in the $Nb_2C_6H_4^+$ cluster. ON stands for the occupation number. The red and blue colours represent the positive value and negative value, respectively. (b) Two-dimensional localized orbital locator-π (LOL-π, unit: eV) analysis of the *ortho*-C_6H_4. A higher LOL-π value indicates a more localized distribution of π-electrons, and the colour depth increases with π-electron density. (c) Electrostatic potentials (ESPs, unit: eV) of the *ortho*-C_6H_4. The maximum and minimum values of the electrostatic potential are shown by the blue and orange spheres, respectively. (d) Interaction region indicator (IRI, unit: eV) of $Nb_2C_6H_4^+$. The isosurface map is 0.55. A stronger chemical strength is indicated by a lower value.

structures of C_6H_4 and Nb_2^+. In addition, we have considered benzyne (*ortho*-C_6H_4) and its isomers (*meta*-C_6H_4 and *para*-C_6H_4) in the $Nb_2C_6H_4^+$ structures (Fig. S3, ESI†), and $Nb_2C_6H_4^+$ given in Fig. 3a and b is the ground state. The dehydrogenation reaction of Nb_2^+ with C_6H_6 has been previously reported, but the detailed reaction mechanism was not given.[64,65]

The adaptive natural density partitioning (AdNDP) method is further applied to determine the bonding character of $Nb_2C_6H_4^+$. Two types of bonds exist in the $Nb_2C_6H_4^+$ cluster: the two-center two-electron (2c–2e) bond in Fig. S4 (ESI†) and the three-center two-electron (3c–2e) bond in Fig. 4a. There are two delocalized 3c–2e π-bonds located on the Nb–Nb–C (Nb–Nb–C2 and Nb–Nb–C3) and Nb–C–C (Nb–C1–C2, Nb–C3–C4, and Nb–C5–C6) units. The Nb2 atom carries most of the unpaired spin density (0.91 *e*) of the $Nb_2C_6H_4^+$ cluster, as shown in Fig. 3b, which provides an ideal site for N_2 adsorption (**I9** in Fig. 3c).

$Nb_2C_6H_4N_2^+$ is observed in the reactions of $Nb_2C_6H_4^+$ and N_2, and the calculated PES is given in Fig. 3c. The reaction pathway commences with the formation of encounter complex **I9** (−0.92 eV), in which the incoming N_2 molecule is adsorbed at the Nb2 atom *via* an η^1-N_2 coordination mode. Subsequently, the Nb1–N2 bond is formed in **I10** (−1.56 eV) by changing the ∠NbNbN from 119° in **I9** to 50° in **I10**. The most stable structure for $Nb_2C_6H_4N_2^+$ is **P1** (−1.98 eV), and the N_2 unit is in a side-on end-on (η^1:η^2) coordination mode. The further N–N bond breaking is kinetically impeded by an intrinsic energy barrier **TS11**. Along the reaction coordinate ($Nb_2C_6H_4^+ + N_2 \rightarrow\rightarrow$ **P1**) in Fig. 3b, the N≡N bond length is significantly elongated from 109 pm in the free N_2 molecule to 121 pm in $Nb_2C_6H_4N_2^+$, suggesting that the N≡N triple bond is activated.

4. Discussion

Based on the experimental results shown in Fig. 1b, Nb^+ is almost inert toward N_2, and this may be due to the fast dissociation rate of N_2 desorption from the encounter complex (6.0×10^9 s^{-1} predicted by variational transition state theory). The dual-metal cation Nb_2^+ greatly enhances the N_2 absorption rate, but this rate is still one order of magnitude smaller than that of $N_2/Nb_2C_6H_4^+$. This interesting phenomenon gives rise to several questions: (1) What is the distinctive characteristic of

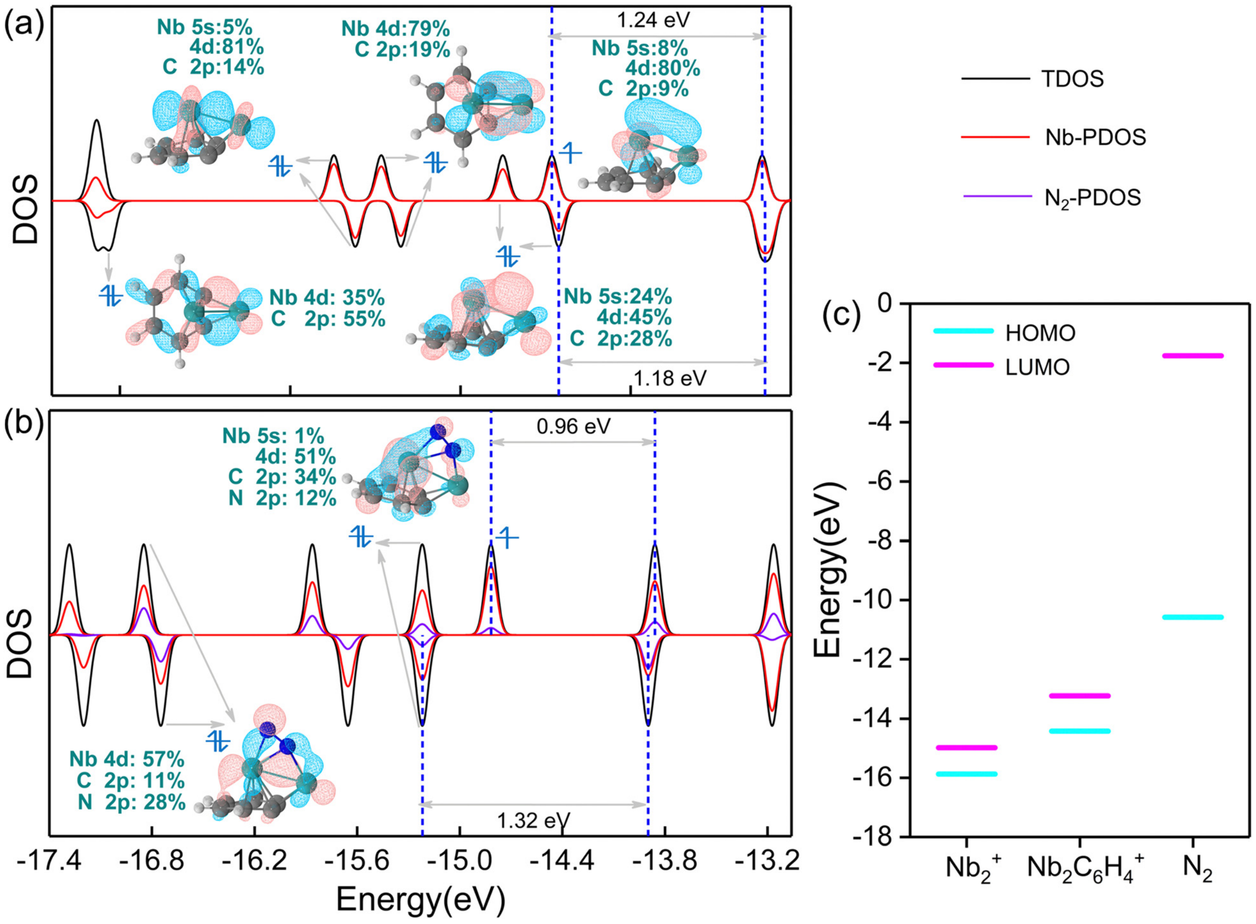

Fig. 5 Total density of states (TDOS, black line) for (a) $Nb_2C_6H_4^+$ and (b) $Nb_2C_6H_4N_2^+$. Projected density of states (PDOS) of Nb (red line) and N_2 (purple line) are also given. In each panel, the HOMO position is indicated by the blue dotted line. The HOMO–LUMO energy gaps are also given. The orbital insets are shown to illustrate the bond interactions between the $Nb_2C_6H_4^+$ cluster and N_2. The corresponding orbital contributions for Nb, C, and N are also presented. (c) The HOMO and LUMO energy levels of Nb_2^+, $Nb_2C_6H_4^+$, and N_2, respectively.

the *ortho*-C_6H_4 ligand? (2) What is the interaction between Nb_2^+ and the *ortho*-C_6H_4 ligand? (3) Why does the *ortho*-C_6H_4 ligand facilitate N_2 absorption?

4.1 Characteristic of the *ortho*-C_6H_4 ligand and interaction between Nb_2^+ and *ortho*-C_6H_4

Inspired by the conjugated π-bond in C_6H_6, the localized orbital locator-π (LOL-π) calculation is employed to visualize the distribution of π-electrons in the *ortho*-C_6H_4 ligand, as shown in Fig. 4b. The deeper colour in the red region indicates a higher distribution of π-electrons. When hydrogen is abstracted from C_6H_6, the C–C bond decreases from 139 pm in C_6H_6 to 125 pm in *ortho*-C_6H_4, leading to the increased π-electrons accumulation on this bond (Fig. 4b). Note that other C–C bonds in *ortho*-C_6H_4 are just as strong as those in C_6H_6. Consequently, the intense π-electrons create the negative electrostatic potential region, as depicted in Fig. 4c. The region with the lowest electrostatic potential (−0.65 eV) is situated on the C–C bond, which favors Nb_2^+ bonding.

Based on the natural population analysis (NPA) charges of the $Nb_2C_6H_4^+$ cation, the electron (0.72 *e*) transfers from the Nb_2^+ unit to the *ortho*-C_6H_4 ligand. The interaction region indicator (IRI) analysis (Fig. 4d) reveals the formation of a strong chemical bond (green region) between Nb and C atoms. The bonding character and mechanism are further examined using the density of states (DOS) and the frontier orbital analyses, as shown in Fig. 5 and Fig. S6 (ESI†). In Fig. 5a, the 4d-electrons of Nb dominate the DOS around the HOMO. The Nb-4d and C-2p orbitals have strong interaction in the Nb–C bond, as demonstrated by the β-HOMO orbital, as well as the HOMO−1, HOMO−2, and HOMO−3 in both α and β orbitals.

Notably, several significant changes are induced when the Nb_2^+ bonds with *ortho*-C_6H_4. (1) The unpaired spin density (UPSD) distribution is adjusted. In $^4Nb_2^+$, the UPSD is evenly distributed over each Nb atom (1.50 *e*), whereas the UPSD is localized on one Nb atom (0.91 *e*) in $^2Nb_2C_6H_4^+$. (2) A polar $Nb_2C_6H_4^+$ cluster is formed. The dipole moment is increased from 0 D for Nb_2^+ to 3.5 D for $Nb_2C_6H_4^+$. The vector direction in $Nb_2C_6H_4^+$ (the blue arrow in $Nb_2C_6H_4^+$, Fig. 3b) is along an axis perpendicular to the Nb–Nb bond, lying in the Nb1–*O*–Nb2 plane. Large dipole moment favors electron transfer and N_2 adsorption. (3) The HOMO energy level is raised from −15.87 eV in Nb_2^+ to −14.42 eV in $Nb_2C_6H_4^+$ (Fig. 5c), which is closer to the LUMO of N_2 (−1.76 eV).

4.2 Interaction between $Nb_2C_6H_4^+$ and N_2

In $Nb_2C_6H_4N_2^+$ and $Nb_2N_2^+$, N_2 molecules are stably adsorbed on the Nb atoms in terms of side-on end-on (η^1:η^2) coordination mode. The adsorption energy of N_2 on $Nb_2C_6H_4^+$ (−1.98 eV) is larger than that of Nb_2^+/N_2 (−1.01 eV), which is consistent with experimental observations.

As shown in Fig. 5a and Fig. S6a (ESI†), the HOMO of $Nb_2C_6H_4^+$ is closer to the LUMO in N_2, compared with that of the Nb_2^+ cation, resulting in a higher reactivity towards N_2. The frontier orbital analyses for $Nb_2N_2^+$ and $Nb_2C_6H_4N_2^+$ cations are performed in Fig. 5b and Fig. S6b (ESI†). As electron donors, Nb atoms directly interact with N_2, and the obvious orbital interaction between Nb-4d and N-2p is shown in Fig. 5b (*e.g.*, the α-HOMO−1 and α-HOMO−3) and Fig. S6b (ESI,† *e.g.*, the α-HOMO−3 and α-HOMO−6). The back-donating electrons from the Nb-4d orbital to the antibonding π*-orbital of N_2 activate the N≡N triple bond. The key factor in enhancing the N_2 adsorption rate stems from the addition of the *ortho*-C_6H_4 ligand, forming a polar $Nb_2C_6H_4^+$ cluster. The positive-N1 (0.14 *e*) and negative-N2 (−0.15 *e*) charges in **I9** indicate that N_2 has been slightly polarized. A strong interaction occurs between the polarized N_2 and the polar $Nb_2C_6H_4^+$. In the condensed-phase system, increasing the polarity of the solid surface can increase the adsorption capacity of polar gas molecules.[66,67] Therefore, increasing the polarity of gas-phase clusters favors non-polar N_2 adsorption.

In Fig. 6, the natural population analysis charges of Nb, and N atoms, as well as the *ortho*-C_6H_4 ligand along the reaction coordinates of the $Nb_2C_6H_4^+/N_2$ system are carried out. In the course of **R** →→ **P1**, two Nb atoms and the *ortho*-C_6H_4 ligand act as an electron reservoir, transferring 0.53 *e* to N2. In the formation of encounter complex **I9** (**R** → **I9**), the N1 atom releases negative charges (ΔQ = 0.14 *e*) to the Nb2 and N2 atoms, forming the Nb2–N2 bond. Then negative charges flow from two Nb atoms to the N2 unit (ΔQ = 0.52 *e*), leading to the formation of the Nb1–N2 bond (**I9** → **I10**). In the last step for the formation of the Nb1–N1 bond (**I10** → **P1**), the N2 atom donates 0.16 *e* to the Nb1 and N1 atoms. In a word, although the *ortho*-C_6H_4 ligand in $Nb_2C_6H_4^+$ seems like a spectator and does not contribute electrons to the reaction, its presence is significant in increasing polarity, raising the HOMO energy

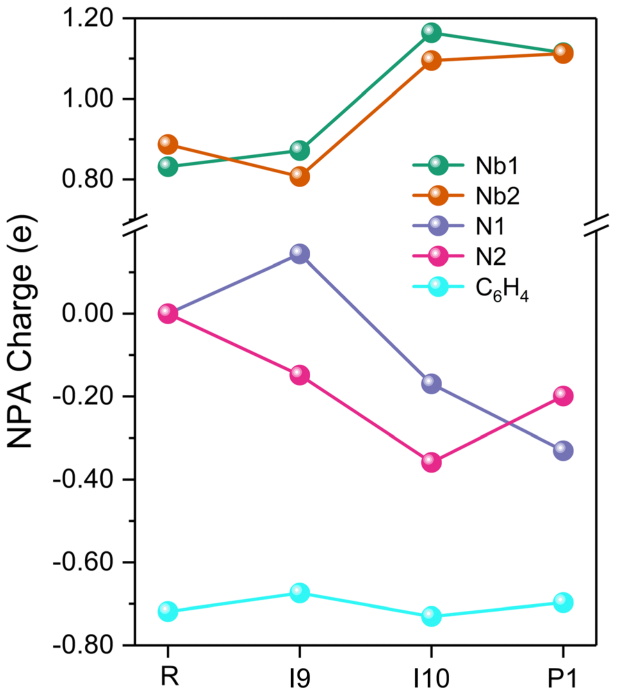

Fig. 6 Natural population analysis (NPA) charges on the Nb, N atoms, and *ortho*-C_6H_4 ligand along reaction coordinates of N_2 activation on the $Nb_2C_6H_4^+$ cation.

level, and increasing the N_2 adsorption energy. These behaviors facilitate N_2 adsorption. In addition, $Nb_2C_6H_4N_2^+$ has more vibrational degrees of freedom than $Nb_2N_2^+$ does, and therefore the former has more chance to be stabilized in the experiment.

5. Conclusions

In summary, the gas-phase reaction of Nb_2^+ with C_6H_6 is identified, which releases one H_2 molecule. The N_2 adsorption activity mediated by three different cations, that is, Nb^+, Nb_2^+, and $Nb_2C_6H_4^+$, under thermal collision conditions has been investigated using mass spectrometry experiments and theoretical calculations. The experimental results indicate that the reaction rate constant of $Nb_2C_6H_4^+/N_2$ is 10 times faster than that of Nb_2^+/N_2, suggesting that organic ligand *ortho*-C_6H_4 facilitates N_2 adsorption, while the reaction rate of Nb^+/N_2 is quite low under similar reaction conditions. Using DFT calculations, the electron transfer, chemical bonding, and orbital interaction mechanisms have been investigated between Nb_2^+ and *ortho*-C_6H_4. In $Nb_2C_6H_4^+$, the enhanced polarity as well as the raised HOMO level facilitate N_2 adsorption. The present gas-phase study provides molecular level insight into the mechanism of N_2 adsorption mediated by metal active sites with organic ligands.

Author contributions

Feng-Xiang Zhang: conceptualization, data curation, formal analysis, investigation, methodology, software, validation, visualization, writing – original draft and writing – review and editing. Yi-Heng Zhang and Ming Wang: data curation, formal analysis, methodology and validation. Jia-Bi Ma: conceptualization, formal analysis, funding acquisition, project administration, resources, supervision and writing – review and editing.

Conflicts of interest

The authors declare no conflict of interest.

Acknowledgements

This work was supported by the National Natural Science Foundation of China (22222301), the Beijing Natural Science Foundation (2222023), the National Key Research and Development Program of China (2021YFA1601800), and the BIT Research and Innovation Promoting Project (2022YCXY029).

Notes and references

1 Q. Zhuo, X. Zhou, T. Shima and Z. Hou, *Angew. Chem., Int. Ed.*, 2023, **62**, e202218606.

2 T. T. Liu, D. D. Zhai, B. T. Guan and Z. J. Shi, *Chem. Soc. Rev.*, 2022, **51**, 3846–3861.

3 L. J. Wu, Q. Wang, J. Guo, J. Wei, P. Chen and Z. Xi, *Angew. Chem., Int. Ed.*, 2023, **62**, e202219298.

4 T. Itabashi, K. Arashiba, A. Egi, H. Tanaka, K. Sugiyama, S. Suginome, S. Kuriyama, K. Yoshizawa and Y. Nishibayashi, *Nat. Commun.*, 2022, **13**, 6161.

5 X. Shi, Q. Wang, C. Qin, L. J. Wu, Y. Chen, G. X. Wang, Y. Cai, W. Gao, T. He, J. Wei, J. Guo, P. Chen and Z. Xi, *Natl. Sci. Rev.*, 2022, **9**, nwac168.

6 R. J. Burford and M. D. Fryzuk, *Nat. Rev. Chem.*, 2017, **1**, 1–13.

7 L.-H. Mou, Z.-Y. Li and S.-G. He, *J. Phys. Chem. Lett.*, 2022, **13**, 4159–4169.

8 S. Jiang, M.-F. Jardinaud, J. Gao, Y. Pecrix, J. Wen, K. Mysore, P. Xu, S.-C. Carmen, Y. Ruan, M. Zhu, F. Li, E. Wang, P. Poole, P. Gamas and J. D. Murray, *Science*, 2021, **374**, 625–628.

9 M. Wang, J. Ma, Z. Shang, L. Fu, H. Zhang, M. B. Li and K. Lu, *J. Mater. Chem. A*, 2023, **11**, 3871–3887.

10 X. Gao, L. An, D. Qu, W. Jiang, Y. Chai, S. Sun, X. Liu and Z. Sun, *Sci. Bull.*, 2019, **64**, 918–925.

11 M. Reiners, D. Baabe, K. Munster, M. K. Zaretzke, M. Freytag, P. G. Jones, Y. Coppel, S. Bontemps, I. D. Rosal, L. Maron and M. D. Walter, *Nat. Chem.*, 2020, **12**, 740–746.

12 P. Garrido-Barros, J. Derosa, M. J. Chalkley and J. C. Peters, *Nature*, 2022, **609**, 71–76.

13 H. J. Himmel and M. Reiher, *Angew. Chem., Int. Ed.*, 2006, **45**, 6264–6288.

14 X. Xin, I. Douair, Y. Zhao, S. Wang, L. Maron and C. Zhu, *J. Am. Chem. Soc.*, 2020, **142**, 15004–15011.

15 Z. J. Lv, Z. Huang, W. X. Zhang and Z. Xi, *J. Am. Chem. Soc.*, 2019, **141**, 8773–8777.

16 Y. Ohki, K. Munakata, Y. Matsuoka, R. Hara, M. Kachi, K. Uchida, M. Tada, R. E. Cramer, W. M. C. Sameera, T. Takayama, Y. Sakai, S. Kuriyama, Y. Nishibayashi and K. Tanifuji, *Nature*, 2022, **607**, 86–90.

17 C. J. P. J. Talarmin, *Nature*, 1985, **317**, 652–653.

18 S. F. McWilliams, D. L. J. Broere, C. J. V. Halliday, S. M. Bhutto, Q. M. Brandon and P. L. Holland, *Nature*, 2020, **584**, 221–226.

19 S. L. Buchwald, B. T. Watson, R. T. Lum and W. A. Nugent, *J. Am. Chem. Soc.*, 1987, **109**, 7137–7141.

20 S. L. Buchwald and R. B. Nielsen, *Chem. Rev.*, 1988, **88**, 1047–1058.

21 S. J. McLain, R. R. Schrock, P. R. Sharp, M. R. Churchill and W. J. Youngs, *J. Am. Chem. Soc.*, 1979, **101**, 263–265.

22 X. Chen, Z. Xiong, M. Yang and Y. Gong, *Chem. Commun.*, 2022, **58**, 7018.

23 B. Yuan, Z. Liu, X.-N. Wu and S. Zhou, *Sci. China: Chem.*, 2022, **65**, 1720–1724.

24 Y.-Q. Ding, F. Ying, Y. Li, J. Xie and J.-B. Ma, *Inorg. Chem.*, 2023, **62**, 6102–6108.

25 X. Sun, S. Zhou, L. Yue, C. Guo, M. Schlangen and H. Schwarz, *Angew. Chem., Int. Ed.*, 2019, **58**, 3635–3639.

26 R. A. J. O'Hair and G. N. Khairallah, *J. Cluster Sci.*, 2004, **15**, 331–363.

27 Y. Zhao, J.-T. Cui, M. Wang, D. Y. Valdivielso, A. Fielicke, L.-R. Hu, X. Cheng, Q.-Y. Liu, Z.-Y. Li, S.-G. He and J.-B. Ma, *J. Am. Chem. Soc.*, 2019, **141**, 12592–12600.

28 Y.-Q. Ding, Z.-Y. Chen, Z.-Y. Li, X. Cheng, M. Wang and J.-B. Ma, *J. Phys. Chem. A*, 2022, **126**, 1511–1517.

29 M. Wang, H.-Y. Zhou, A. M. Messinis, L.-Y. Chu, Y. Li and J.-B. Ma, *J. Phys. Chem. Lett.*, 2021, **12**, 6313–6319.

30 Y.-Q. Ding, Y. Li, F. Ying, M. Wang and J.-B. Ma, *J. Phys. Chem. Lett.*, 2022, **13**, 492–497.

31 L.-Y. Chu, Y.-Q. Ding, M. Wang and J.-B. Ma, *Phys. Chem. Chem. Phys.*, 2022, **24**, 14333–14338.

32 M. Gao, Y.-Q. Ding and J.-B. Ma, *Int. J. Mol. Sci.*, 2022, **23**, 6976.

33 M. Wang, L.-Y. Chu, Z.-Y. Li, A. M. Messinis, Y.-Q. Ding, L. Hu and J.-B. Ma, *J. Phys. Chem. Lett.*, 2021, **12**, 3490–3496.

34 G.-D. Jiang, Z.-Y. Li, L.-H. Mou and S.-G. He, *J. Phys. Chem. Lett.*, 2021, **12**, 9269–9274.

35 L.-H. Mou, G.-D. Jiang, Z.-Y. Li and S.-G. He, *Chin. J. Chem. Phys.*, 2020, **33**, 507–520.

36 V. I. Baranov, G. Javahery and D. K. Bohme, *Chem. Phys. Lett.*, 1995, **239**, 339–343.

37 R. K. Milburn, V. Baranov, A. C. Hopkinson and D. K. Bohme, *J. Phys. Chem. A*, 1999, **103**, 6373–6382.

38 D. Caraiman and D. K. Bohme, *Int. J. Mass Spectrom.*, 2003, **223–224**, 411–425.

39 X. Cheng, Z.-Y. Li, G.-D. Jiang, X.-X. Liu, Q.-Y. Liu and S.-G. He, *J. Phys. Chem. Lett.*, 2023, **14**, 6431–6436.

40 Y. Zhao, J.-C. Hu, J.-T. Cui, L.-L. Xu and J.-B. Ma, *Chem. – Eur. J.*, 2018, **24**, 5920–5926.

41 H.-Y. Zhou, M. Wang, Y.-Q. Ding and J.-B. Ma, *Dalton Trans.*, 2020, **49**, 14081.

42 Z. Yuan, Z.-Y. Li, Z.-X. Zhou, Q.-Y. Liu, Y.-X. Zhao and S.-G. He, *J. Phys. Chem. C*, 2014, **118**, 14967–14976.

43 Z.-Y. Li, Z. Yuan, X.-N. Li, Y.-X. Zhao and S.-G. He, *J. Am. Chem. Soc.*, 2014, **136**, 14307–14313.

44 M. J. Frisch, G. W. Trucks, H. B. Schlegel, G. E. Scuseria, M. A. Robb, J. R. Cheeseman, G. Scalmani, V. Barone, B. Mennucci, G. A. Petersson, H. Nakatsuji, M. Caricato, X. Li, H. P. Hratchian, A. F. Izmaylov, J. Bloino, G. Zheng, J. L. Sonnenberg, M. Hada, M. Ehara, K. Toyota, R. Fukuda, J. Hasegawa, M. Ishida, T. Nakajima, Y. Honda, O. Kitao, H. Nakai, T. Vreven, J. A. Montgomery, Jr., J. E. Peralta, F. Ogliaro, M. Bearpark, J. J. Heyd, E. Brothers, K. N. Kudin, V. N. Staroverov, T. Keith, R. Kobayashi, J. Normand, K. Raghavachari, A. Rendell, J. C. Burant, S. S. Iyengar, J. Tomasi, M. Cossi, N. Rega, J. M. Millam, M. Klene, J. E. Knox, J. B. Cross, V. Bakken, C. Adamo, J. Jaramillo, R. Gomperts, R. E. Stratmann, O. Yazyev, A. J. Austin, R. Cammi, C. Pomelli, J. W. Ochterski, R. L. Martin, K. Morokuma, V. G. Zakrzewski, G. A. Voth, P. Salvador, J. J. Dannenberg, S. Dapprich, A. D. Daniels, O. Farkas, J. B. Foresman, J. V. Ortiz, J. Cioslowski and D. J. Fox, *Gaussian 09, Revision D.01*, Gaussian, Inc., Wallingford CT, 2013.

45 Y. Zhao and D. G. Truhlar, *J. Chem. Phys.*, 2006, **125**, 194101.

46 Y. Li, M. Wang, Y.-Q. Ding, C.-Y. Zhao and J.-B. Ma, *Phys. Chem. Chem. Phys.*, 2021, **23**, 12592–12599.

47 Q. Chen, Y.-X. Zhao, L.-X. Jiang, H.-F. Li, J.-J. Chen, T. Zhang, Q.-Y. Liu and S.-G. He, *Phys. Chem. Chem. Phys.*, 2018, **20**, 4641–4645.

48 S. Grimme, J. Antony, S. Ehrlich and H. Krieg, *J. Chem. Phys.*, 2010, **132**, 154104.

49 B. Attila, A. M. Steven and Z. Z. Marek, *J. Phys. Chem. A*, 1998, **102**, 6340–6347.

50 F. Weigend and R. Ahlrichs, *Phys. Chem. Chem. Phys.*, 2005, **7**, 3297–3305.

51 R. Krishnan, J. S. Binkley, R. Seeger and J. A. Pople, *J. Chem. Phys.*, 1980, **72**, 650–654.

52 T. Clark, J. Chandrasekhar, G. W. Spitznagel and P. V. R. Schleyer, *J. Comput. Chem.*, 1983, **4**, 294–301.

53 R. Ditchfield, W. J. Hehre and J. A. Pople, *J. Chem. Phys.*, 1971, **54**, 724–728.

54 J. L. Bao and D. G. Truhlar, *Chem. Soc. Rev.*, 2017, **46**, 7548–7596.

55 E. D. Glendening, C. R. Landis and F. Weinhold, *J. Comput. Chem.*, 2013, **34**, 1429–1437.

56 T. Lu and F. Chen, *J. Comput. Chem.*, 2012, **33**, 580–592.

57 T. Lu and Q. Chen, *Theor. Chem. Acc.*, 2020, **139**, 25.

58 T. Lu and S. Manzetti, *Struct. Chem.*, 2014, **25**, 1521–1533.

59 T. Lu and Q. Chen, *Chem.: Methods*, 2021, **1**, 231.

60 Z. Liu, T. Lu and Q. Chen, *Carbon*, 2020, **165**, 461–467.

61 G. Gioumousis and D. P. Stevenson, *J. Chem. Phys.*, 1958, **29**, 294–299.

62 G. Kummerlöwe and M. K. Beyer, *Int. J. Mass Spectrom.*, 2005, **244**, 84–90.

63 K. Balasubramanian, *J. Chem. Phys.*, 1995, **114**, 10375–10388.

64 C. Berg, T. Schindler, G. Niedner-Schatteburg and V. E. Bondybey, *J. Chem. Phys.*, 1995, **102**, 4870–4884.

65 S. Roszak, D. Majumdara and K. Balasubramaniana, *J. Phys. Chem. A*, 1999, **103**, 5801–5806.

66 F. Mohajer and M. N. Shahrak, *Heat Mass Transfer*, 2019, **55**, 2017–2023.

67 M. R. A. Tourrette, R. H. R. Valentin, M. Boissière, J. M. Devoisselle, F. D. Renzo and F. Quignard, *Carbohydr. Polym.*, 2011, **85**, 44–53.